


Article

Dynamic Simulation of the Temperature Field of LiH Single Crystal Growth

Yingwu Jiang ^{1,2}, Donghua Xie ^{2,3}, Jiliang Wu ², Huan Li ^{2,4}, Jipeng Zhu ², Muyi Ni ¹ , Tao Gao ⁴ and Xiaoqiu Ye ^{2,*}¹ Sino-French Institute of Nuclear Engineering & Technology, Sun Yat-sen University, Zhuhai 519082, China² Science and Technology on Surface Physics and Chemistry Laboratory, Mianyang 621908, China³ Institute of Materials, China Academy of Engineering Physics, Mianyang 621900, China⁴ Institute of Atomic and Molecular Physics, Sichuan University, Chengdu 610000, China

* Correspondence: yexiaoqiu@caep.cn

Abstract: The single-crystal lithium hydride (LiH) generally grows in a gradient temperature region with the Bridgman method. A stable and appropriate temperature gradient is crucial in the crystallization process. In this paper, the temperature variation of single-crystal LiH growth is calculated by the finite element method (FEM). It is shown that the LiH compact melted entirely after heating to 750 °C at 10 °C/min in a dual-temperature furnace and holding for 2.4 h. The crystallization margin was 46.5 °C after holding for 5 h. The crystallization margin of LiH at the cone point, respectively, decreased to 33.7 °C, 28.6 °C, 25.6 °C, and 16.5 °C when the upper furnace was maintained at 750 °C, and lower furnace was cooled to 680 °C, 650 °C, 630 °C, and 550 °C, respectively. The optimal conditions for obtaining large size and high-quality LiH single crystals were predicted to be 630 °C at a lower-temperature-zone, 200 mL/min (cooling water flux), and 20 mm/h rise rate of the furnace. Based on the parameters of the above simulation, we synthesized LiH single crystal. X-ray diffraction (XRD) patterns showed that the LiH single crystal exhibited a (2 0 0) crystallographic plane at 44.5° with good chemical stability in air.

Keywords: LiH; the growth of single crystal; vertical Bridgman method; temperature field



Citation: Jiang, Y.; Xie, D.; Wu, J.; Li, H.; Zhu, J.; Ni, M.; Gao, T.; Ye, X. Dynamic Simulation of the Temperature Field of LiH Single Crystal Growth. *Crystals* **2023**, *13*, 504. <https://doi.org/10.3390/cryst13030504>

Academic Editor: Janis Virbulis

Received: 19 February 2023

Revised: 9 March 2023

Accepted: 10 March 2023

Published: 15 March 2023



Copyright: © 2023 by the authors. Licensee MDPI, Basel, Switzerland. This article is an open access article distributed under the terms and conditions of the Creative Commons Attribution (CC BY) license (<https://creativecommons.org/licenses/by/4.0/>).

1. Introduction

LiH, as an excellent hydrogen storage material [1,2], an ideal neutron moderator [3,4], a strong reducing agent [5–7], and a potential fusion fuel [8], has been widely studied since it was successfully prepared in 1896. However, the purity can only reach 94% because of the deliquescence [9–11]. The single crystal growth purifies the LiH sample and enriches the primary physical property database. Moreover, large-size single crystals also have essential application in the optical field [12].

The preparation of single-crystal LiH has been reported by hydrogenizing lithium film with atomic hydrogen, the Bridgman–Stockbarger technique, and the Czochralski method [13,14]. Pretzel et al. prepared single LiH in 1959 by slow crystallization of melt under hydrogen gas at moderate pressure. Then, the physical, chemical, and thermal properties were tested [12,15–17]. Holcombe grew single LiH with the Stockbarger technique, and the product contained 0.2 wt% impurity [13]. Tyutyunnik et al. prepared a large single LiH with a modified Bridgman–Stockbarger method using ultrasound, while the temperature field distribution was not given [14]. The Bridgman method is the most commonly used for large, complex crystal growth. It has many advantages [18–20]: 1. The shape of the crucible can be designed to meet the practical requirements. 2. The crystal can be grown directionally by pre-treatment at crucible bottom. 3. The simple growth process can be automated and programmed.

The growth of single-crystal LiH is a prolonged process. A high-quality single crystal could be ensured and human resources and material could be fully used if the temperature field distribution for a new device had been simulated. This work simulates the temperature

field during the growth of a single-crystal LiH with the Bridgeman method. The significant factors affecting the temperature field were analyzed, such as the temperature in the lower furnace, the cooling water flow rate, and the furnace's rising rate. In addition, the LiH single crystal is characterized by XRD and SEM.

2. Experimental Device and Simulation Model

2.1. Bridgeman Device

The single crystal growth system is a non-standard equipment designed by the Science and Technology on Surface Physics and Chemistry Laboratory. It is mainly composed of a dual-temperature furnace, a servo system, a stainless-steel reactor, an iron crucible, a copper water cooler, a vacuum system, and a data acquisition system, as shown in Figure 1.

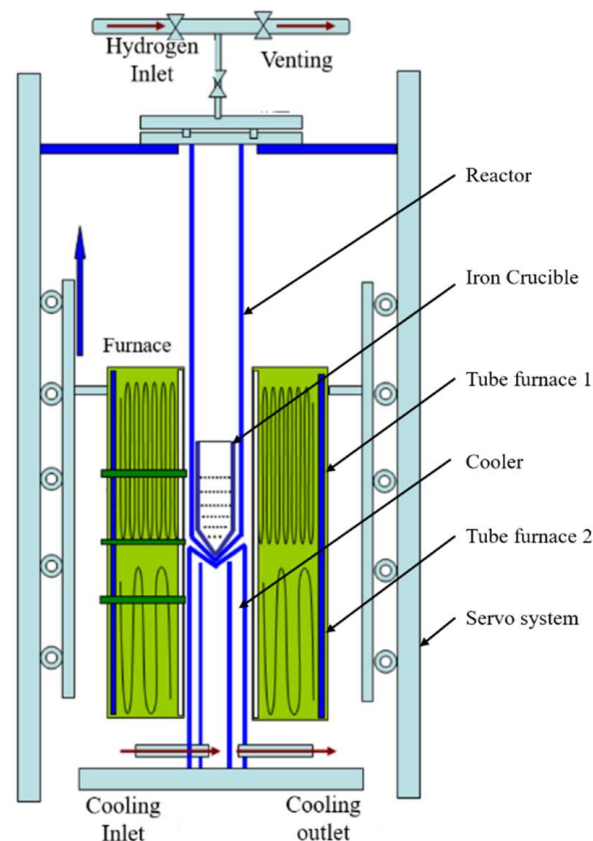


Figure 1. Schematic diagram of LiH single crystal growth device.

The single-crystal LiH growth is based on the Bridgman method [13,15]. The polycrystal LiH first melts at 750 °C under 400 kPa hydrogen protection. Then, the crucible tip is cooled, and the liquid begins to crystallize. Finally, the furnace rises slowly, and a temperature gradient promotes the growth of single-crystal LiH.

The specific process is shown in Figure 2, which mainly includes:

- (1) The polycrystal LiH *compact* was placed in a pure iron crucible under low humidity and low oxygen condition, and the crucible was placed in a 316 L stainless steel reactor.
- (2) The reactor was first evacuated and filled with 400 kPa hydrogen. Then, the furnace was heated to 750 °C, and heat was preserved to melt the LiH completely.
- (3) The lower furnace was slowly cooled to a specific temperature (T , °C), and the cooling water was injected to make the LiH nucleate at the cone point.
- (4) The servo system launched to make the furnace rise slowly. Then, a temperature gradient was formed, and LiH was gradually solidified along the length direction.

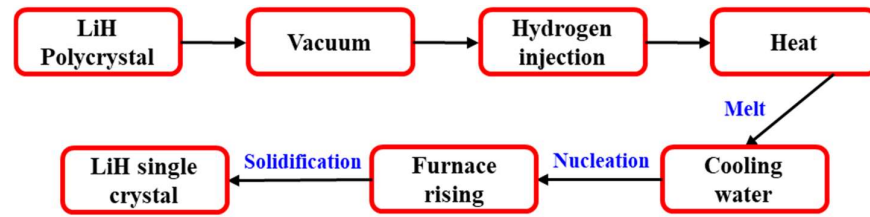


Figure 2. Lithium hydride single crystal growth process.

2.2. Simulation Model and Parameters

The experimental device is modeled based on the experimental design. The reactor, crucible, cooler, furnace, and other customized instruments all have axisymmetric properties, and the symmetry axes coincided during the experiment. For this reason, a two-dimensional symmetric model was built to reduce the computational expense, as shown in Figure 3. The reactor and crucible all have a 45° apex angle, which can be entirely fitted under ideal conditions. However, there are some errors because of installation and device coordination. Then, it was believed there was a 1–2 mm gap between the two tips.

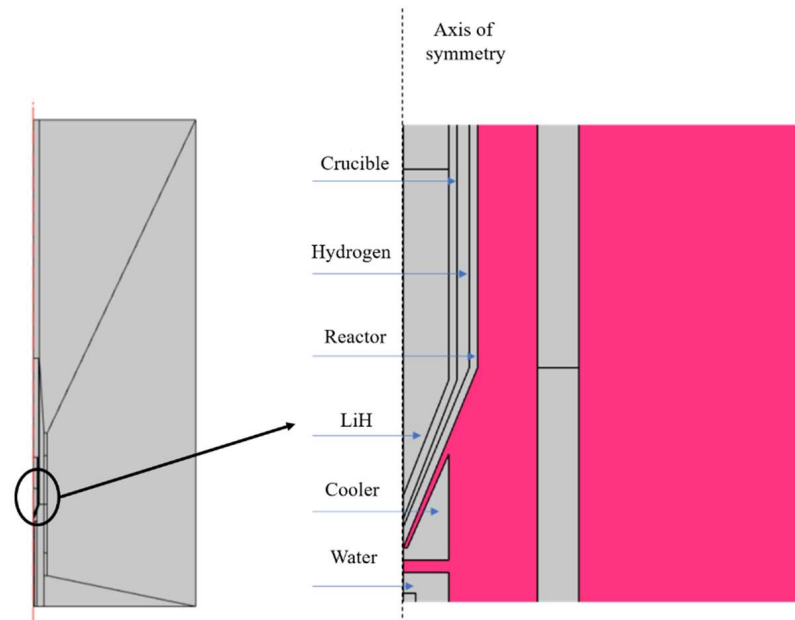


Figure 3. Two-dimensional axisymmetric geometry diagram for LiH single crystal growth device.

The airflow in the furnace and hydrogen movement in the reactor is driven by a temperature gradient, which could be considered incompressible laminar flow [21]. The cooling water flows in a turbulent form because of the 180° rotation in the cooler. The heat interchange between the furnace and the reactor conducts through the air, where the heat radiation is ignored. Heat conduction and thermal convection were considered between LiH, crucible, reactor, and hydrogen.

There is a strong coupling between the temperature field and the flow field. Heat convection and conduction work together in a fluid medium, but only heat conduction affects temperature field distribution in solid material. Equation (1) [22–24] shows the control equation of the temperature field.

$$\rho C_p \frac{\partial T}{\partial t} + \delta \rho C_p \vec{u} \cdot \nabla T - \nabla \cdot (-k \nabla T) = 0 \quad (1)$$

$$\delta = \begin{cases} 0, & \text{solid} \\ 1, & \text{liquid} \end{cases} \quad (2)$$

where ρ is the material density, C_p is the heat capacity at constant pressure, \vec{u} is the fluid flow rate, k is the thermal conductivity, and T is the Kelvin temperature.

The Navier–Stokes equation is to describe the airflow, as shown in formula (3).

$$\rho \frac{\partial \vec{u}}{\partial t} + \rho (\vec{u} \cdot \nabla) \vec{u} = \nabla \cdot [-pI + K] + F \quad (3)$$

where I is the unit vector, K is the viscous stress tensor, and F is the volumetric force.

The essential physical parameters of LiH, pure Fe, 316 L stainless steel, copper, air, and hydrogen used in the calculation are derived from the database of COMSOL. The specific parameters are shown in Figure 4. The geometric characteristics and physical properties of the growth system are shown in Table 1.

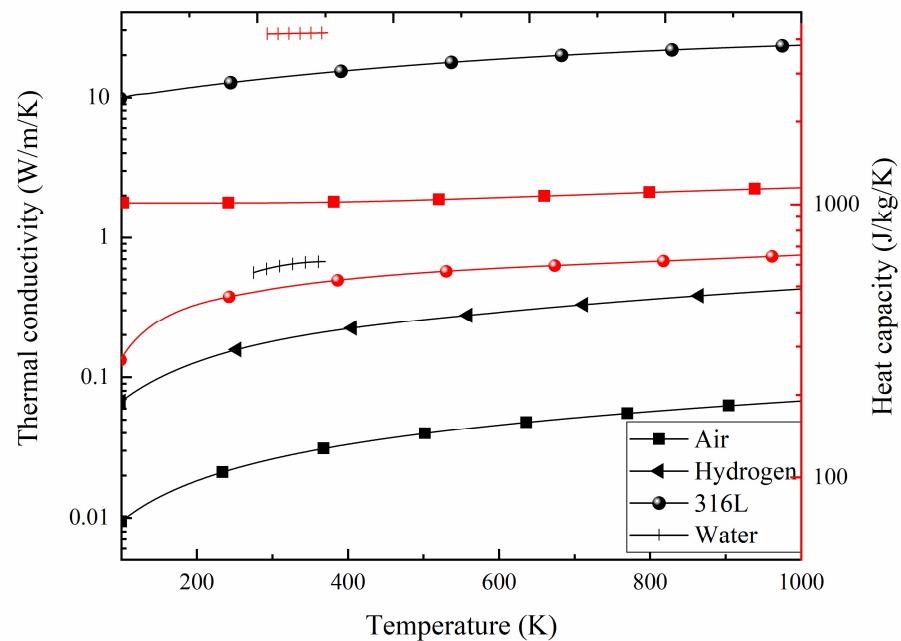


Figure 4. Valuable physical property data used in simulation.

Table 1. Parameters of crystal growth system.

Parameter	Symbol (Unit)	Value
Ampoule length	L1 (mm)	450
Ampoule outer diameter	D1 (mm)	36
Ampoule thickness	T1 (mm)	2
Crucible outer diameter	D2 (mm)	28
Crucible thickness	T2 (mm)	2
Furnace chamber radius	D3 (mm)	65
Hydrogen condition	P (kPa)	400

3. Result and Discussion

3.1. The Temperature Field in Melting

The furnaces were heated uniformly from room temperature (20 °C) to 750 °C at 10 °C/min and then held for 750 °C. Heat is transferred through furnace-air-reactor-hydrogen-crucible-(hydrogen)-LiH. The heat transfer is driven by a temperature gradient, which needs time to fully melt LiH.

The air temperature in the furnace continuously rises in heating and heat preservation. Eddy currents are formed around the furnace due to the temperature gradient, as shown in Figure 5. The maximal velocity is in the furnace with a disordered temperature field.

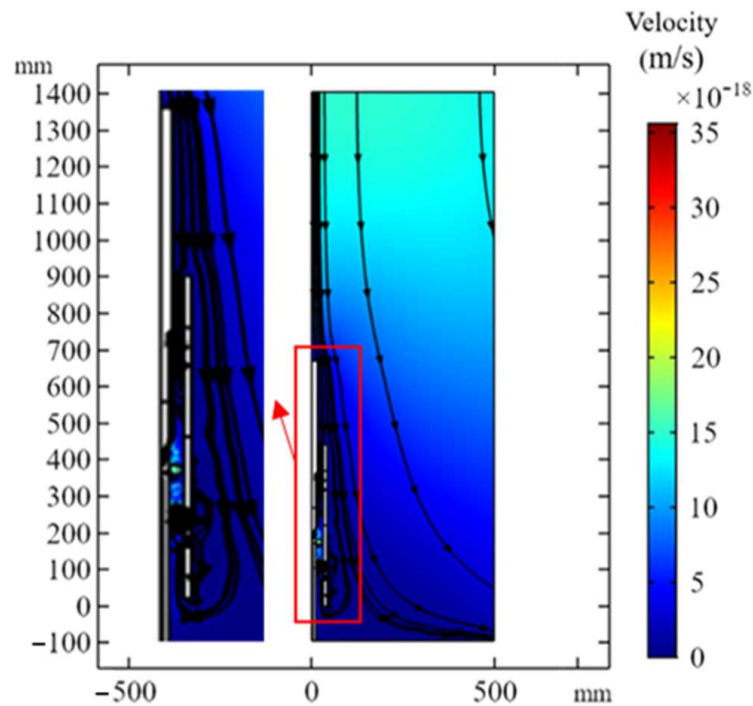


Figure 5. The airflow field and flow line around the furnace.

The flow outside the furnace is laminar, which circles the furnace and takes heat away. A large amount of heat is discharged from the upper and lower ports by continuous air exchange. The temperature field shown in Figure 6 is in a “gourd” shape with the synergistic effect of airflow and the furnace’s outer thermal insulation layer when thermal equilibrium arrives in heat preservation. Moreover, the temperature 50 cm away from the furnace did not fluctuate significantly during the experiment under natural convection.

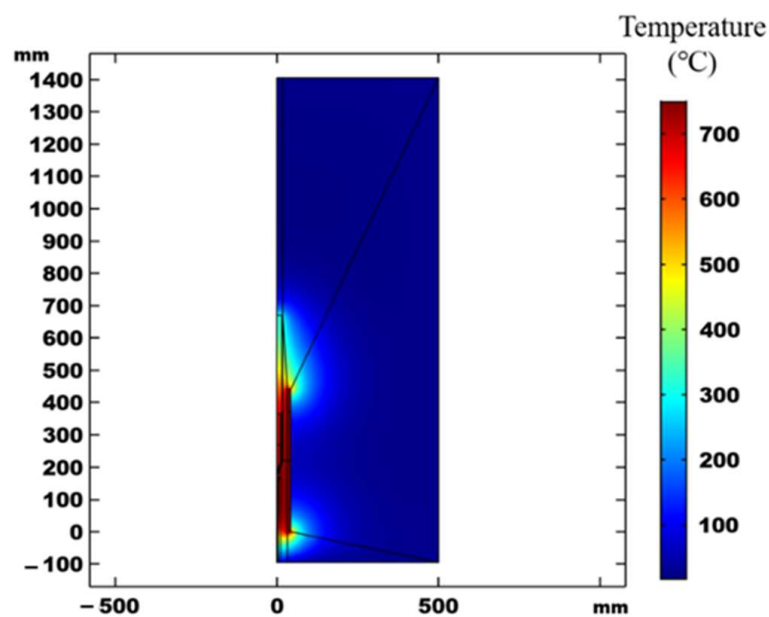


Figure 6. Schematic diagram of temperature field at heat preservation thermal equilibrium.

Heat is transferred through furnace-air-reactor-hydrogen-crucible-(hydrogen)-LiH in heating. The LiH temperature at the cone point (contact point between LiH and crucible tip) rose slowly in the first two hours because it was the farthest from the heat source. The

primary heat transfer medium is air, leading to considerable thermal resistance. For this reason, the highest temperature was distributed at the upper end of the sample where there is less air. The temperature in the furnace reached about 550 °C two hours later. A lot of heat will be discharged into air, thus reducing the heating efficiency. The reactor is in the upper furnace. For this reason, the heat retention effect at the lower end of the sample was better than the upper. Therefore, the heating rate at the cone point was gradually higher than elsewhere at about 2.5 h, showing two high-temperature regions. The maximal temperature finally showed at the cone point as this phenomenon gradually intensified, and the result is shown in Figure 7. Moreover, there is a narrow gap between the reactor and the furnace and a fully covered furnace. Then, the temperature gradient was negligible in the radial direction when the thermal equilibrium arrived.

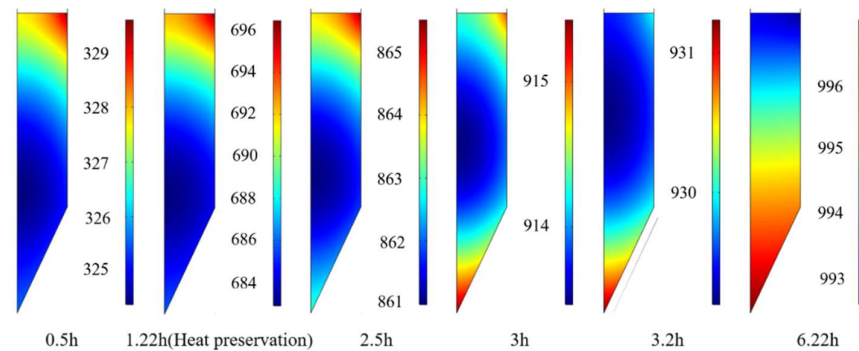


Figure 7. The temperature field of LiH during heating and the heat preservation process (T[K]).

The temperature variation at the LiH cone point is shown in Figure 8 in heating and heat preservation. There was a delay in LiH temperature due to the slow heat transfer in the first 10 min. The temperature difference between LiH and the furnace's inner wall was enormous (300–600 °C) at the beginning of heat preservation. Then, the heat flow had an immense transmission power, and the LiH temperature rose rapidly. The temperature difference gradually decreased, showing a slow-growth trend. The LiH crystal reached the melting point (680 °C) after holding for 2.0 h, 2.4 h, and 2.8 h at the heating rate of 5 °C/min, 10 °C/min, and 25 °C/min, respectively, and they all can reach 722.3 °C after holding for 5 h.

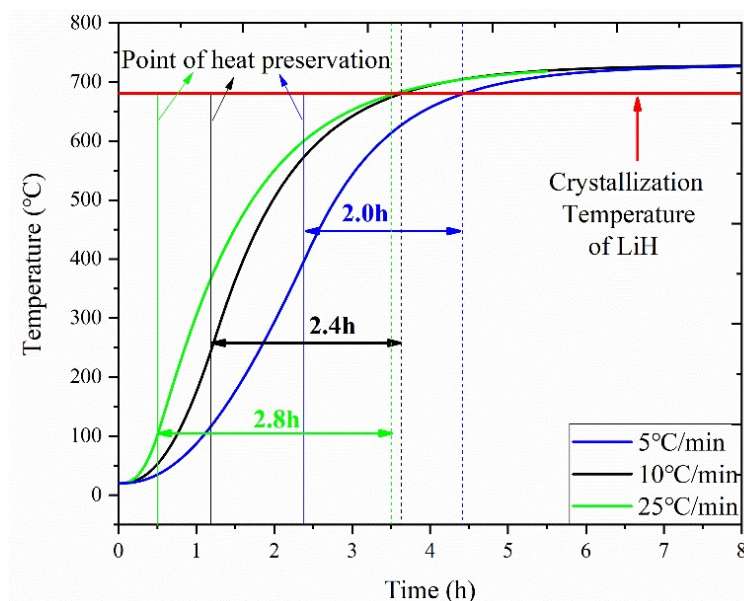


Figure 8. The temperature of LiH at the conical point during heating and heat preservation at a different heating rate.

It can be seen that if the furnace was heated to 750 °C at 5 °C/min, 10 °C/min, and 25 °C/min, respectively, and at least 2.0 h, 2.4 h, and 2.8 h hours should be set in the heat preservation stage to ensure the total melt of LiH compact. The latent heat and experimental operating margin should be considered in the experiment, so the heat preservation time must be appropriately extended.

3.2. Effect of Temperature Distribution in the Lower Furnace

A temperature decline of 10 °C/min is usually used for cooling during the experiment. Therefore, it needs 20 min, 12 min, 10 min, and 7 min when the lower furnace is 550 °C, 630 °C, 650 °C, and 680 °C, respectively. The furnace cooling process was ignored in the simulation since the time required for heat balance after cooling is much longer than the cooling time. The lower furnace was directly adjusted to 550 °C, 630 °C, 650 °C, and 680 °C after heat preservation. The specific temperature distribution at the inner wall of the furnace is expressed by Equation (4). The temperature variation of the lower furnace broke the thermal balance in the furnace. Thus, the LiH sample temperature began to drop, and the variation at LiH cone points was monitored, as shown in Figure 9.

$$f(z) = \begin{cases} T, & \text{if } z \in (70, 95 + \frac{(T+273.15)}{6}) \\ T + 6 \times (z - (220 - \frac{(750-T)}{6})), & \text{if } z \in (95 + \frac{(T+273.15)}{6}, 220) \\ 750, & \text{if } z \in (220, 370) \end{cases} \quad (4)$$

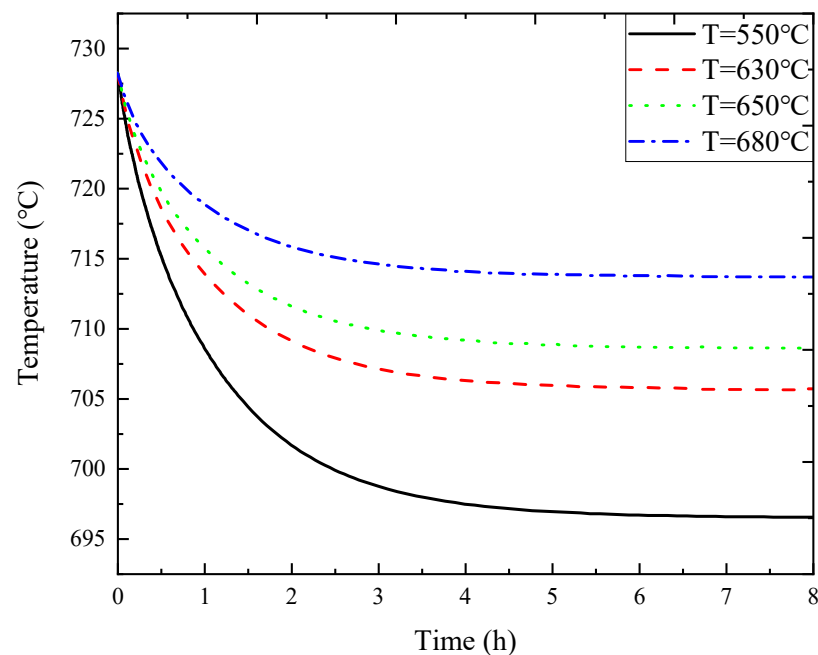


Figure 9. The temperature of LiH at the conical point during cooling of the lower furnace.

The cone point is in a superheated state when the thermal balance is again reached, and the temperatures are, respectively, 696.5 °C, 705.6 °C, 708.6 °C, and 713.7 °C. All the temperatures are higher than the melting point of LiH, which is conducive to the subsequent temperature rise of the furnace. The cooling water will cause a large area of undercooling condensation if the crystal margin is too small, which would influence the quality of the LiH single crystal. For this reason, T should not be smaller than 550 °C.

The temperature at the furnace's central axis is shown in Figure 10. The figure is divided into seven areas from left to right corresponding to the air gap, copper cooler, hydrogen gap, reactor, crucible, LiH, and hydrogen above the LiH, which fully shows the temperature distribution of the main structure in the furnace chamber. The lowest air gap is located in the upper third of the lower-temperature zone, and LiH is distributed in

the upper-temperature zone. Figure 10 shows that the metal, such as the copper cooler, 316 L reactor, and pure iron crucible, have a small thermal resistance, and the temperature difference on both sides is within 5 °C. However, the gap filled with air and hydrogen has a considerable thermal resistance and a noticeable temperature difference.

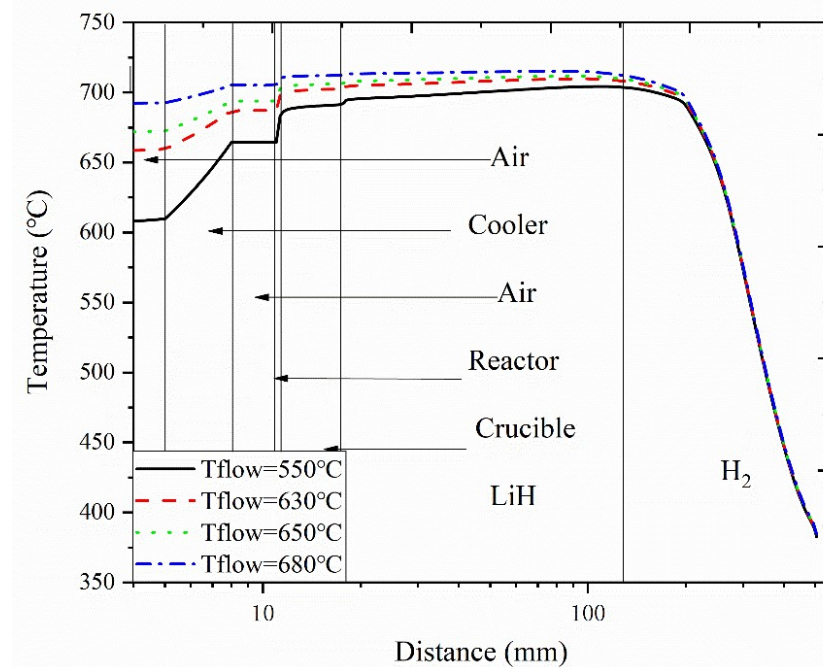


Figure 10. The temperature distribution in the central axis of the furnace.

In summary, there is a certain crystal margin when T drops from 750 °C to 550 °C, 630 °C, 650 °C, and 680 °C. However, T should not be too small to ensure a small LiH undercooling area when cooling water is injected.

3.3. Effect of Cooling Water

Under the condition of 750 °C in the upper furnace and 630 °C in the lower furnace, the servo motor functions too slowly to lift the electric heating furnace with 5 mm/h after the furnace system reaches thermal balance. At the same time, the cooling water circulation device starts. The relative geometric position of the furnace and reactor was fixed during the simulation, and the furnace rising was realized by changing the temperature boundary condition on the inner wall of the furnace, which is shown in Equation (5).

$$f_T(z, t) = f(z - V \times t) \quad (5)$$

where f is the temperature distribution of the furnace after cooling in the lower furnace, as shown in Equation (4). V is the furnace rise rate, t is time, and z is z -coordinate.

LiH will be completely located in the lower furnace after the furnace rises 100 mm. The influence of cooling water flow on the LiH temperature field was studied at a 5 mm/h rising rate. The cooling water flow was 0 L/min, 0.001 L/min, 0.005 L/min, 0.01 L/min, 0.05 L/min, and 0.2 L/min. The temperature variation at the LiH cone point was observed under both rising and cooling effects, and the specific results are shown in Figure 11.

The furnace rises slowly at 5 mm/h. LiH is entirely in the lower furnace after 20 h, and condensation crystallization is completed. The horizontal coordinate is the rising distance of the furnace in Figure 11. The LiH temperature at the cone point changes almost linearly when there is no cooling water. The LiH tip reaches the crystallization temperature when the furnace rises 45 mm (9 h later), then solidifies gradually; 0.001 L/min cooling water is too small which has little influence on the LiH temperature. The crystallization point can be reached after rising 41 mm (8.2 h later), about one hour earlier than

without cooling water. The heat dissipation is considerable and dramatically influences the LiH temperature field when the cooling water flow reaches 0.005 L/min. The heat taken away by cooling water is more significant than that provided by the furnace, resulting in the rapid decline of LiH temperature. The system reaches a new thermal equilibrium about 2 h later, and the LiH temperature decreases linearly. The crystallization temperature at the LiH cone point is reached while the furnace rises 7.5 mm (1.5 h). The crystallization speed is greatly accelerated by 7.5 h in advance compared with the condition without cooling water; 0.05 L/min is almost the cooling flow threshold, where the cooling effect reached a perfect state. However, the local boiling phenomenon might occur if the cooling flux is not big enough, resulting in the cooling efficiency decline quickly in the experiment. So, the cooling water flow should be greater than 0.05 L/min at a 5 mm/h rising rate.

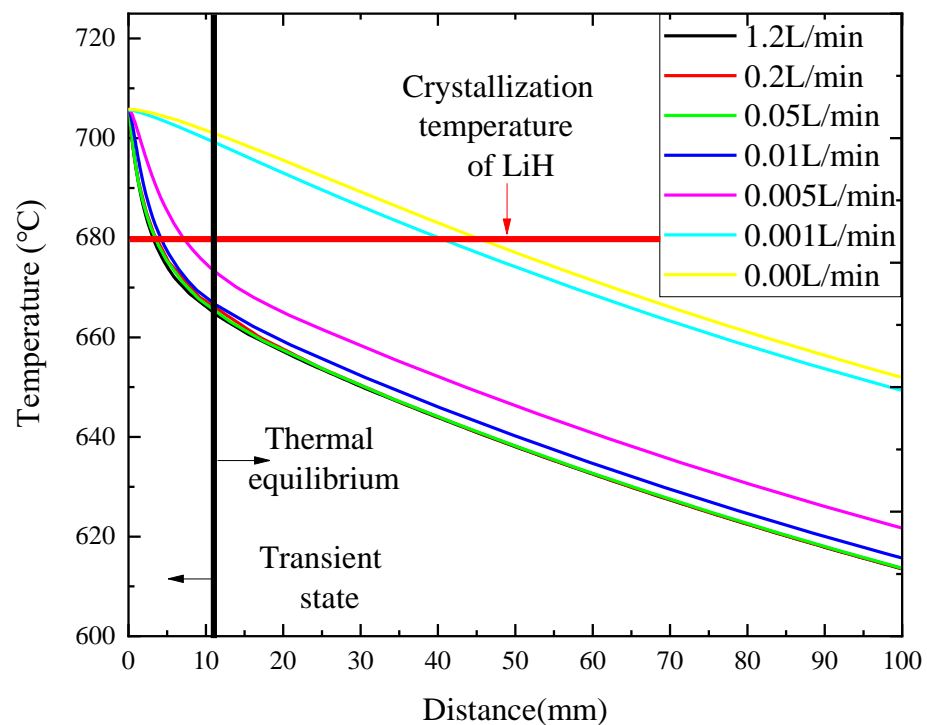


Figure 11. The temperature variation of the LiH conical point at different flow flux.

3.4. Effect of Furnace Rising Rate

The furnace moves 100 mm with different rising rates at 0.2 L/min cooling water. Figure 12a shows the temperature at the cone point linked with the upward distance of the furnace. The LiH cone point reaches the crystallization temperature when the furnace moves up 0.7 mm, 3.4 mm, 6.5 mm, and 12 mm at 1 mm/h, 5 mm/h, 10 mm/h, and 20 mm/h, respectively. The LiH temperature field gradually reaches thermal equilibrium under the synergistic effect of furnace rising and cooling water. The characteristic time to reach the balance correlates with the upward rate. The temperature at the LiH cone point changes synchronously at different moving rates in the first 1.4 h, where the cooling water plays a leading role in heat dissipation. The relative geometry position of the crucible and furnace is more and more significant as the furnace rises. For this reason, the temperature at different rising rates is gradually separated, as shown in Figure 12b. Meanwhile, the LiH cooling rate positively correlates with the rising furnace rate.

Minor environmental perturbation and less temperature variation rate are more conducive to forming larger grains in crystallization [25]. The study shows that cooling water injection causes an enormous temperature gradient. Therefore, a 20 mm/h rising rate could be set to save the experimental cost if environmental perturbation could be controlled.

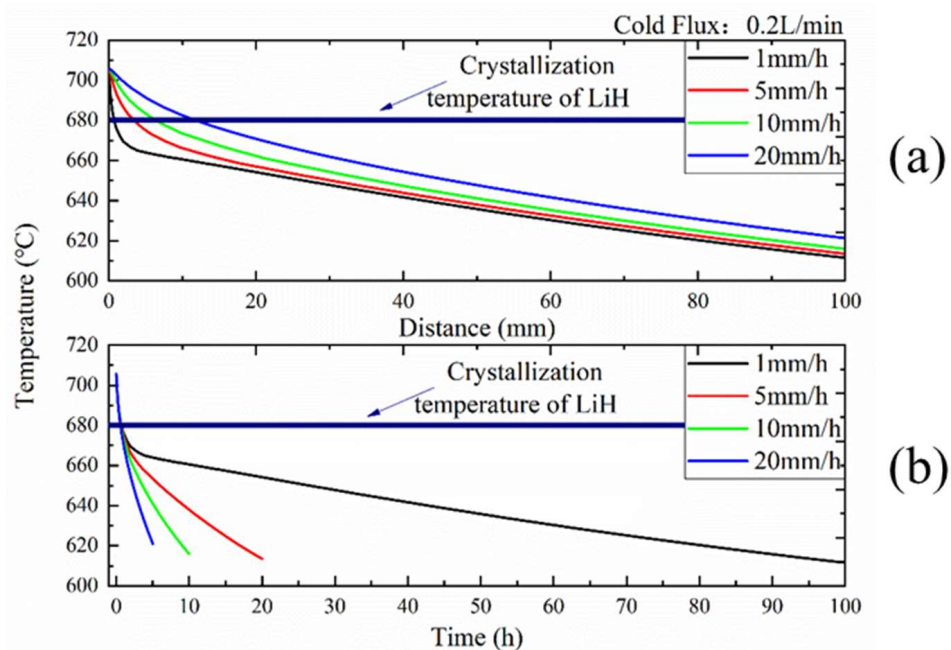


Figure 12. The temperature variation at the LiH conical point at different rise speed. (a) is for the upward distance of furnace and (b) is for the time furnace moved.

4. Characterization of LiH Crystal

The polycrystalline LiH is stored in a glove box where the water and oxygen content are less than 1 ppm, and the temperature is maintained at 15 °C. LiH is easy to react with H₂O and CO₂ in air, and long-term storage would lead to surface deliquescence. The polycrystalline LiH is grey because its surface is covered by hydrolysate, as shown in Figure 13(a1), while this alkali metal hydride is a colorless solid. The XRD pattern in Figure 14 was tested by DX-2700BH X-ray Diffractometer, which is equipped with a Cu target to generate 1.540538 Å ($\lambda_{\alpha 1}$) and 1.544324 Å ($\lambda_{\alpha 2}$) X-ray. The step size and time per step were 0.017°, 0.4178°/s, respectively. It proves that the polycrystalline LiH contains hydrolysate, such as LiOH, Li₂O, LiOH(H₂O), and Li₂CO₃.

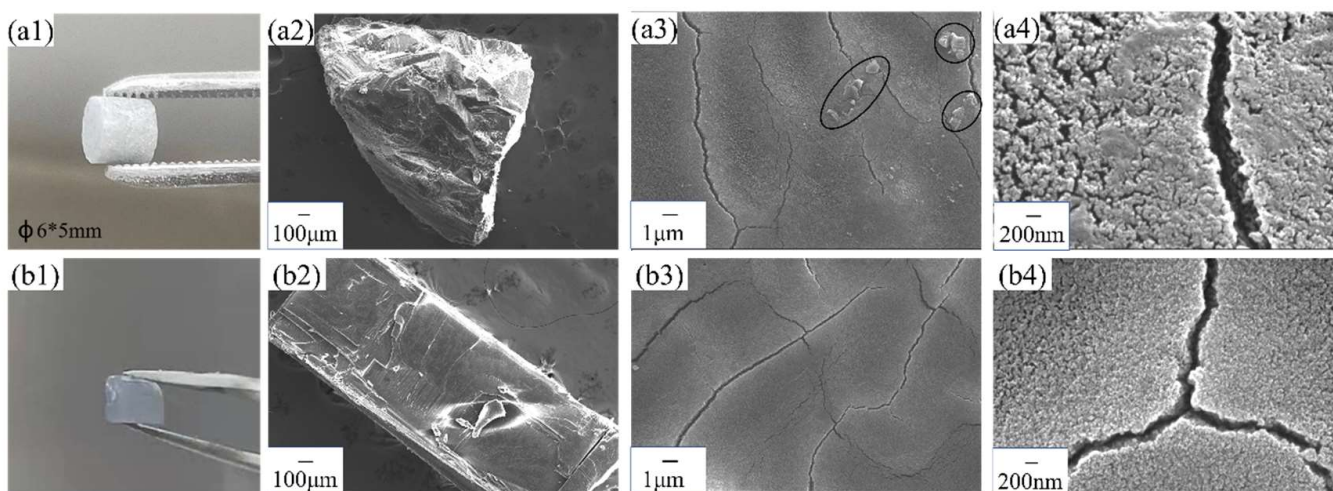


Figure 13. (a1) Polycrystalline LiH partical, (a2), (a3), (a4) are SEM of polycrystalline LiH with scaleplate of 100 μm , 1 μm , 1 nm, respectively; (b1) Single crystal LiH partical, (b2), (b3), (b4) are SEM of Single crystal LiH with scaleplate of 100 μm , 1 μm , 1 nm, respectively.

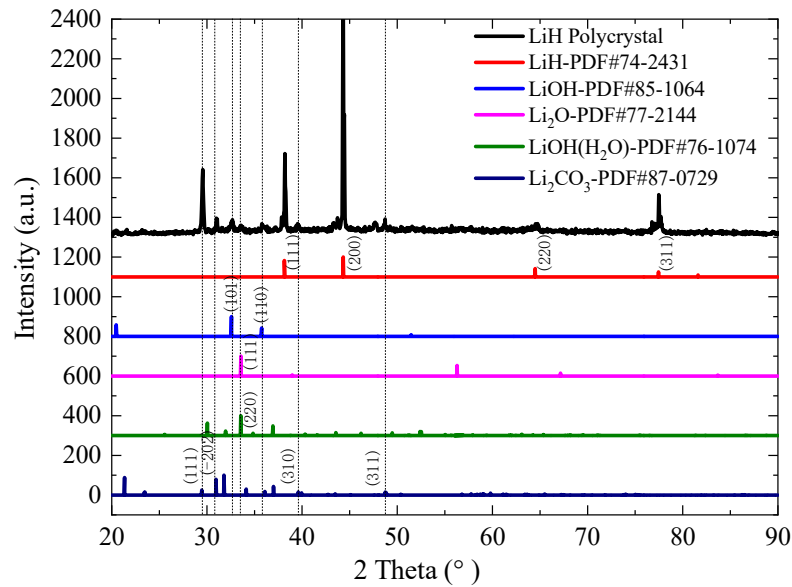


Figure 14. XRD pattern of polycrystalline LiH.

LiH polycrystalline materials were melted and recrystallized to produce single-crystal products by the aforementioned method. The size of a single LiH is consistent with the crucible. However, it is easy to break when LiH and crucible are separated. Figure 13(b1) shows the LiH single crystal has a smoother surface than polycrystalline, and the microstructure also reveals this phenomenon. Clastics are randomly distributed on polycrystalline in Figure 13(a3), while LiH single crystal shows a clean surface. Moreover, the grains of LiH single crystal are granular and homogeneous in Figure 13(b4), whereas the grains are adhesive because of the deliquescence in Figure 13(a4). Figure 15 is the XRD pattern of single LiH, showing only two parallel crystal planes between 20 and 120°, (200) and (400). It confirms that the aforementioned method is meaningful for single-crystal growth. In addition, it also suggests that the LiH single crystal exhibits good chemical stability in air.

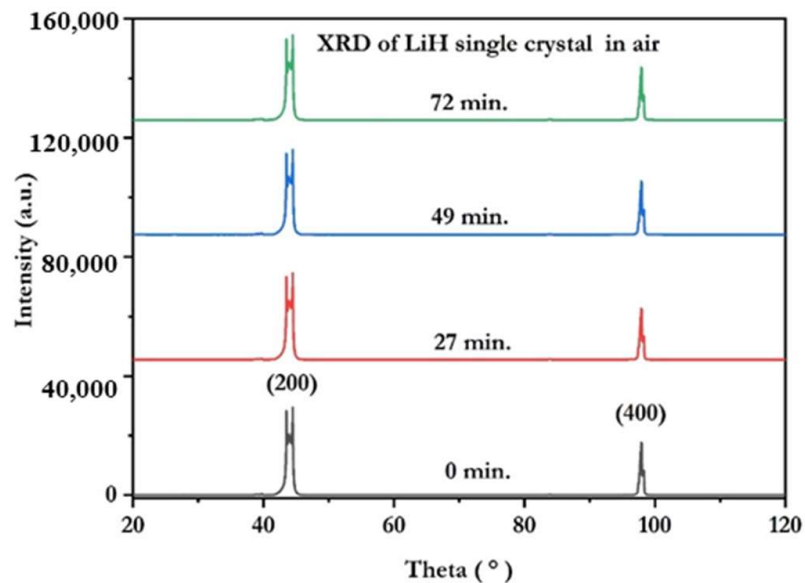


Figure 15. XRD pattern of LiH single crystal in air.

5. Conclusions

The effects of temperature in the lower-temperature zone, cooling water, and furnace upshift rate on the LiH growth temperature field were simulated. The results show that the heat preservation should, respectively, be set at least 2.0 h, 2.4 h, and 2.8 h to ensure the total melt of LiH billet when the furnace is heated to 750 °C at 5 °C/min, 10 °C/min, and 25 °C/min, respectively. The LiH temperature field's crystallization margin would not be enough to ensure a small undercooling area when cooling water is passed if the lower-temperature-zone T is too low (almost <550 °C). A 50 mL/min cooling water could achieve a favorable cooling effect and can be increased appropriately to avoid local boiling in the experiment. The temperature gradient caused by the up-moving rate of the furnace is less critical than that of cooling water, so a 20 mm/h up-moving rate could ensure the crystallization quality and save the experimental cost. In addition, the XRD pattern shows that the LiH single crystal exhibits a (2 0 0) crystallographic plane at 44.5° and good chemical stability in air.

Author Contributions: Conceptualization, X.Y. and M.N.; methodology, Y.J., X.Y. and J.W.; software, Y.J., J.Z. and H.L.; validation, X.Y.; formal analysis, T.G.; investigation, Y.J., D.X., J.W. and H.L.; resources, X.Y. and M.N.; data curation, Y.J.; writing—original draft preparation, Y.J.; writing—review and editing, Y.J.; visualization, Y.J. and H.L.; supervision, X.Y.; project administration, X.Y.; funding acquisition, X.Y. All authors have read and agreed to the published version of the manuscript.

Funding: The funds supported this work from Science and Technology on Surface Physics and Chemistry Laboratory, China (No. WDZC202103 and No. 6142A02200206) and Magnetic Confinement fusion Energy Research Project (2015GB109002).

Data Availability Statement: The data that support the findings of this study are available within this article.

Conflicts of Interest: The authors declare no conflict of interest.

References

- Schlapbach, L.; Züttel, A. Hydrogen-storage materials for mobile applications. *Nature* **2001**, *414*, 353–358. [[CrossRef](#)] [[PubMed](#)]
- Schlapbach, L. Hydrogen as a Fuel and Its Storage for Mobility and Transport. *MRS Bull.* **2002**, *27*, 675–679. [[CrossRef](#)]
- Chugunov, I.N.; Shevelev, A.E.; Gin, D.B.; Kiptily, V.G.; Gorini, G.; Nocente, M.; Tardocchi, M.; Doinikov, D.N.; Naidenov, V.O.; Khilkevitch, E.M. Development of gamma-ray diagnostics for ITER. *Nucl. Fusion* **2011**, *51*, 083010. [[CrossRef](#)]
- Montgomery, C.D. Fabrication and properties of lithium hydride. *Nucl. Eng. Des.* **1973**, *25*, 309–314. [[CrossRef](#)]
- Wang, P.; Chang, F.; Gao, W.; Guo, J.; Wu, G.; He, T.; Chen, P. Breaking scaling relations to achieve low-temperature ammonia synthesis through LiH-mediated nitrogen transfer and hydrogenation. *Nat. Chem.* **2017**, *9*, 64–70. [[CrossRef](#)] [[PubMed](#)]
- Kubota, K.; Kaneko, T.; Hirayama, M.; Yonemura, M.; Imanari, Y.; Nakane, K.; Kanno, R. Direct synthesis of oxygen-deficient $\text{Li}_2\text{MnO}_{3-x}$ for high capacity lithium battery electrodes. *J. Power Sources* **2012**, *216*, 249–255. [[CrossRef](#)]
- Michaely, A.; Janka, O.; Gießelmann, E.C.; Haberkorn, R.; Wiedemann, H.T.; Kay, C.W.; Kickelbick, G. Black Titania and Niobia within Ten Minutes—Mechanochemical Reduction of Metal Oxides with Alkali Metal Hydrides. *Chem.—A Eur. J.* **2023**, e202300223. [[CrossRef](#)]
- Haertling, C.; Hanrahan, R.; Smith, R. A literature review of reactions and kinetics of lithium hydride hydrolysis. *J. Nucl. Mater.* **2006**, *349*, 195–233. [[CrossRef](#)]
- Ren, R.; Ortiz, A.L.; Markmaitree, T.; Osborn, W.; Shaw, L.L. Stability of Lithium Hydride in Argon and Air. *J. Phys. Chem. B* **2006**, *110*, 10567–10575. [[CrossRef](#)]
- Haertling, C.; Hanrahan, R.J.; Wang, Y.; Wetteland, C. Ion Beam Analyses of Moisture Reaction for Single Crystal Lithium Deuteride. *MRS Adv.* **2020**, *5*, 549–558. [[CrossRef](#)]
- Haertling, C.L.; Hanrahan, R.J.; Tesmer, J.R. Hydrolysis Studies of Polycrystalline Lithium Hydride. *J. Phys. Chem. C* **2007**, *111*, 1716–1724. [[CrossRef](#)]
- Pretzel, F.; Rushing, C. Properties of lithium hydride—II optical absorption by color centers. *J. Phys. Chem. Solids* **1961**, *17*, 232–245. [[CrossRef](#)]
- Holcombe, C.E., Jr.; Johnson, D.H. Lithium hydride single crystals. *J. Cryst. Growth* **1973**, *19*, 53–57. [[CrossRef](#)]
- Tyutyunnik, O.; Shulgin, B.; Oparin, D.; Pilipenko, G.; Gavrilov, F.; Tyutyunnik, V. Lithium hydride single crystal growth by bridgman-stockbarger method using ultrasound. *J. Cryst. Growth* **1984**, *68*, 741–746. [[CrossRef](#)]
- Pretzel, F.E.; Rupert, G.N.; Mader, C.L.; Storms, E.K.; Gritton, G.V.; Rushing, C.C. Properties of lithium hydride I. Single crystals. *J. Phys. Chem. Solids* **1960**, *16*, 10–20. [[CrossRef](#)]

16. Lewis, W.; Pretzel, F. Properties of lithium hydride—III. Paramagnetic resonance of color centers. *J. Phys. Chem. Solids* **1961**, *19*, 139–146. [[CrossRef](#)]
17. Pretzel, F.; Gritton, G.; Rushing, C.; Friauf, R.; Lewis, W.; Waldstein, P. Properties of lithium hydride—IV. *J. Phys. Chem. Solids* **1962**, *23*, 325–337. [[CrossRef](#)]
18. Jin, M.; Bai, X.; Tang, Z.; Zhao, S.; Chen, Y.; Zhou, L.; Peng, Y.; Chen, X.; Xu, X. Fabrication of InSb crystal via Horizontal Bridgman method and investigation on its thermoelectric properties. *Mater. Res. Bull.* **2021**, *142*, 111411. [[CrossRef](#)]
19. Chen, H.; Ge, C.; Li, R.; Wang, J.; Wu, C.; Zeng, X. Growth of lead molybdate crystals by vertical Bridgman method. *Bull. Mater. Sci.* **2005**, *28*, 555–560. [[CrossRef](#)]
20. Cröll, A.; Volz, M.P. Detached Bridgman growth—A standard crystal growth method with a new twist. *MRS Bull.* **2009**, *34*, 245–250. [[CrossRef](#)]
21. Liu, J.; Yao, G.; Cui, H.; Dong, S. Evolution of solid-liquid Interface of CdZnTe Growth by Vertical Bridgman Method. *J. Synth. Cryst.* **2003**, *32*, 555–562.
22. Dupret, F.; Nicodème, P.; Ryckmans, Y.; Wouters, P.; Crochet, M. Global modelling of heat transfer in crystal growth furnaces. *Int. J. Heat Mass Transf.* **1990**, *33*, 1849–1871. [[CrossRef](#)]
23. Virzi, A. Computer modelling of heat transfer in Czochralski silicon crystal growth. *J. Cryst. Growth* **1991**, *112*, 699–722. [[CrossRef](#)]
24. Ma, W.; Zhao, L.; Ding, G.; Yang, Y.; Lv, T.; Wu, M.; Liu, L. Numerical study of heat transfer during sapphire crystal growth by heat exchanger method. *Int. J. Heat Mass Transf.* **2014**, *72*, 452–460. [[CrossRef](#)]
25. Kusama, T.; Omori, T.; Saito, T.; Kise, S.; Tanaka, T.; Araki, Y.; Kainuma, R. Ultra-large single crystals by abnormal grain growth. *Nat. Commun.* **2017**, *8*, 354. [[CrossRef](#)] [[PubMed](#)]

Disclaimer/Publisher’s Note: The statements, opinions and data contained in all publications are solely those of the individual author(s) and contributor(s) and not of MDPI and/or the editor(s). MDPI and/or the editor(s) disclaim responsibility for any injury to people or property resulting from any ideas, methods, instructions or products referred to in the content.